Journal of
Materials Chemistry A

Accepted Manuscript

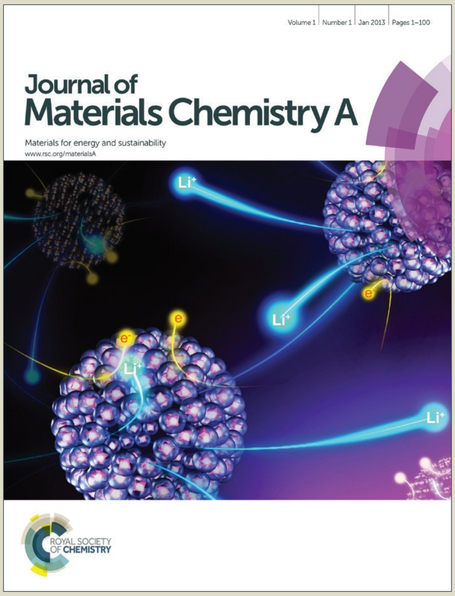

ROYAL SOCIETY
OF CHEMISTRY

www.rsc.org/materialsA

Self-assembly of Mesoporous $ZnCo_2O_4$ Nanomaterials: Density Functional Theory Calculation and Flexible All-Solid-State Energy Storage

Deyang Zhang,[a] Yihe Zhang,*[a] Xiaowei Li,[a] Yongsong Luo,[b] Hongwei Huang,[a] Jiaping wang[c] and Paul K. Chu[d]

[a]*Beijing Key Laboratory of Materials Utilization of Nonmetallic Minerals and Solid Wastes, National Laboratory of Mineral Materials, School of Materials Science and Technology, China University of Geosciences, Beijing, 100083, PR China*

[b]*School of Physics and Electronic Engineering, Xinyang Normal University, Xinyang 464000, P. R. China*

[c]*Department of Physics and Tsinghua-Foxconn Nanotechnology Research Center, Tsinghua University, Beijing 100084, China*

[d]*Department of Physics & Materials Science, City University of Hong Kong, Tat Chee Avenue, Kowloon, Hong Kong, China*

Abstract

Ternary spinel metal oxide $ZnCo_2O_4$ with Co^{2+} at the tetrahedral sites (8a) in the spinel Co_3O_4 replaced by Zn^{2+} is promising in energy storage and an economical way to fabricate low-toxicity nanostructured $ZnCo_2O_4$ is described. Theoretical calculation confirms the rationality of the experimental scheme and elucidates the underlying reason for the increased band gap. The high electrochemical activity and excellent stability of the $ZnCo_2O_4$ NFs//$ZnCo_2O_4$ NWs symmetrical device suggest large potential in energy storage applications. The fabricated device boasts a capacity of 220.6 F g^{-1} at a current density of 2 A g^{-1} and long-term cycling stability with 67.5% of the capacitance retained after 8,000 cycles. The maximum energy density of 60.04 Wh kg^{-1} at a power density of 1.4 KW kg^{-1} and power density of 7 KW kg^{-1} at an energy density of 23.72 Wh kg^{-1} are achieved at an operating voltage of 1.4 V. This combined experimental and theoretical study provides insights to the design and controllable preparation of nanomaterials for energy storage applications.

Keywords: Flexible supercapacitors; $ZnCo_2O_4$; Density Functional Theory; Self-assembly

* To whom correspondence should be addressed: E-mail: zyh@cugb.edu.cn

1. Introduction

On the heels of the fast development of light and flexible portable electronic devices such as rollup displays, smart electronics, and wearable devices, research on efficient flexible energy storage and conversion devices is becoming very important. In addition, the fast-growing market for hybrid vehicles requires further improvement of the power and energy density of energy storage devices [1-11]. Supercapacitors (SCs) as one of the promising energy storage devices have attracted considerable attention for their high power density, fast recharge ability, good rate performance, and long life time[12-19]. Previous studies demonstrate that the type and structures of the electrode materials determine the performance of SCs. Although carbon continues to be the dominant electrode materials in commercial SCs, these devices cannot meet the stringent requirements for future large-scale applications [1], [20-22]. Accordingly, there is much effort to identify better materials, for instance, transition metal oxides, conducting polymers, and hybrid composites, to obtain better specific capacitance and cycle performance [23-29].

Studies on binary metal oxide (MO) like Co_3O_4 show that the materials possess high capacitance and excellent cycle life but there are also disadvantages such as low conductivity, toxic cobalt and high cost thereby impeding adoption in high-performance energy storage devices [20, 30]. To improve the conductivity, Co_3O_4 can be incorporated with conductive materials such as carbon nanotubes, graphene, carbon fibers, or other carbon-based materials. For example, Yu et al. [31] have produced a scrolled structure of Co_3O_4/r-GO by a two-step surfactant-assisted method. The Co_3O_4/r-GO exhibits a large specific capacitance of 163.8 F g^{-1} at a current density of 1 A g^{-1}, which is about 13 times larger than that of pure Co_3O_4. Zhang et al. [32] have used an electrodeposition method to fabricate free-standing Co_3O_4 nanosheet arrays on carbon fiber paper without a polymer binder and the materials show enhanced specific capacity and cycling performance. Another method is to replace the metal ions in the binary MO partially to form a ternary iso-structureby incorporating compatible metals such as Zn, Cu, Mg, and Fe. This process reduces the cost and toxicity while the electrochemical performance is not affected significantly.

Ternary spinel metal oxide $ZnCo_2O_4$ with Co^{2+} at the tetrahedral sites (8a) in the spinel Co_3O_4 replaced by Zn^{2+} (Figure1) poses a cost-effective, scalable, and environmental friendly material suitable for energy storage [30]. Shen et al. [33] have fabricated hierarchical $ZnCo_2O_4$ nanorods on nickel foam by a scalable solution approach and they deliver good electrochemical performance in SCs including high specific capacitance (~1400 F g^{-1} at 1 A g^{-1}), excellent rate capability (72.5% capacity retention at 20 A g^{-1}), and good cycling stability (only 3% loss after 1,000 cycles at 6 A g^{-1}). Luo et al.[34] have employed a cost-effective and simple strategy to prepare hierarchical $ZnCo_2O_4$@MnO_2 nanocomposite on Ni foam and the unique structure has specific capacitances of 2,339 and 1,526 F g^{-1} at current densities of 1 and 10 A g^{-1}, respectively, besides long-term capacity retention of 95.9% after 3,000 cycles at 2 A g^{-1} and 94.5% after 8,000 cycles at 10 A g^{-1}. However, in spite of recent advance, the devices still fall short in meeting the ever-increasing demand of the modern electronics and hybrid vehicle industry.

In this work, mesoporous $ZnCo_2O_4$ nanomaterials with high electric conductivity were produced on the flexible substrate. The cost and the toxicity of the materials are reduced by substitute Co^{2+} with Zn^{2+} at the tetrahedral sites (8a) in the spinel Co_3O_4. The high electrical conductivity and flexible substrate improve the flexibility, mechanical resilience, volume change, weight, and environmental friendliness [35, 36] thereby enabling convenient roll-to-roll processing [37] and fabrication of collapsible and portable SCs.

To evaluate the rationality of the experimental scheme, first-principles calculation based on the density functional theory (DFT) was employed and the electronic structure of Co_3O_4 and $ZnCo_2O_4$ were investigated. In our view, DFT employed here is badly needed as the calculation results could guide us to design a more reasonable experimental plan and to the best of our knowledge, there were no similar reports have been found. This combined experimental and theoretical study provides insights to the design and controllable preparation of nanomaterials for energy storage applications.

2. Experimental Section

Synthesis of $ZnCo_2O_4$ nanoflowers ($ZnCo_2O_4$NFs) on nickel-plated metal fibers and $ZnCo_2O_4$ nanowires ($ZnCo_2O_4$NWs) on carbon fibers

The $ZnCo_2O_4$ NFs were fabricated by a simple hydrothermal method. The nickel-plated metal fibers with dimensions of 1.5 cm × 4 cm were cleaned with 6 M HCl ultrasonically for 30 min to remove the NiO surface layer and then rinsed with deionized (DI) water. In the typical procedures, 1.5 mmol $Zn(NO_3)_2.6H_2O$, 3 mmol $Co(NO_3)_2.6H_2O$, and 2 mmol fluoride NH_4F and 6 mmol $CO(NH_2)_2$ were dissolved in 40 ml of DI water and stirred for 30 min. The solution and the cleaned nickel plated metal fibers were transferred to a 50 ml Teflon-lined stainlesssteel autoclave which was heated to130 ^{o}C for 5h. After the autoclave was cooled to ambient temperature, the samples were removed, washed with distilled water, and dried at 60 ^{o}C. Afterwards, the samples were annealed at 400 ^{o}C in air for 3 h to obtain the $ZnCo_2O_4$ NFs. The $ZnCo_2O_4$ NWs were prepared similarly except that the substrate was changed to carbon fibers.

Materials Characterization

The structure and phase of the products were determined by X-ray diffraction (XRD) performed on a D8 Advance (Germany, Bruker) automated X-ray diffractometer system with CuK_α ($\lambda = 1.5406$ Å) radiation at 40 kV and 40 mA between 10° and 80° at room temperature. The chemical composition was determined by X-ray photoelectron spectroscopy (XPS, PHI 5600 XPS system). Scanning electron microscopy (SEM) was performed on the HITACHI S-4800 microscope (Japan). Transmission electron microscopy (TEM) were carried out on the JEOL JEM-2010 in the bright field and HR-TEM JEM-2010FEF at 200 kV. The Raman scattering spectra were acquired on the WITEC CRM200 equipped with a 532 nm laser source and 50×objective lens. The nitrogen adsorption–desorption isotherms of the samples were measured by using a ASAP 2020 porosimeter at 77 K, and the specific surface area and mesopore size distribution were calculated using the BET and BJH methods.

Electrochemical measurement based on three-electrode supercapacitors testing configuration

The electrochemical tests were conducted by CHI 660E electrochemical workstation (CH Instruments Inc., Shanghai) with a typical three-electrode cell with the as-prepared sample as the working electrode, Pt foil as the counter electrode and Ag/AgCl electrode as the reference electrode, and 2 M KOH as the electrolyte. Cyclic voltammery (CV) tests were measured between 0 and 0.8 V at various scan rates ranging from 2 to 50 mV s^{-1} at room temperature. The galvanostatic charge/discharge tests were conducted between 0 and 0.8 V at various current densities of 2-10 A g^{-1}. The electrochemical impedance spectroscopy (EIS) measurements were performed by applying an alternate current voltage with 5 mV amplitude in a frequency range from 0.01 Hz to 100 kHz at open circuit potential.

Electrochemical measurement of the all-solid-state supercapacitors device

The electrochemical measurements were conducted on the CHI 660E electrochemical workstation (CH Instruments Inc., Shanghai). To fabricate the symmetrical SC prototype, a two-electrode device consisting of $ZnCo_2O_4$ NFs and $ZnCo_2O_4$ NWs as the electrodes was setup. The PVA/KOH gel electrolyte was prepared by adding 2.0 g of PVA and 2.0 g of KOH to 30 mL of H_2O. The mixture was stirred at 80 ^oC until the solution became clear. Two pieces of the electrodes were immersed in the PVA/KOH solution for 2 min, taken out, and assembled leaving aside the bare carbon and nickel-plated metal fibers as the electrode. After solidification at room temperature, the symmetrical capacitor was prepared. The experiments were conducted at room temperature. The specific capacitance (F g^{-1}) and current density (A g^{-1}) were calculated from the total mass of the active materials. Cyclic voltammetry (CV) was performed at a scanning rate of 5~100 mV s^{-1} from 0 to 1.4 V at room temperature and the galvanostatic charging-discharging measurements were performed from 0 to 1.4 V at current densities between 2 and 10 A g^{-1}.

First-principles calculation

To calculate the electronic structures of Co_3O_4 and $ZnCo_2O_4$, first-principles calculations were carried out with the spin-polarized Generalized Gradient Approximation (GGA) by adopting the Perdew-Burkee-Ernzerh (PBE) of exchange-correlation parameterization to Density Functional Theory (DFT) incorporating the LDA+U formalism using the CASTEP program [38]. The plane-wave basis with a kinetic energy cutoff of 400.0 eV and the Monkhorst-Pack grid with 4×4×4 k-point mesh for the integration in the Brillouin zone were used, and the value of the smearing was 0.2 eV. The electronic minimization parameter of the total energy/atom convergence tolerance was 5.0×10^{-6} eV.

3. Results and Discussion

Figure 2 shows the DFT results of the spinel $ZnCo_2O_4$. Figure 2a ($ZnCo_2O_4$) and Figure S1a (Co_3O_4) show that the band gap of Co_3O_4 increases slightly from 1.357 eV to 1.663 eV when Zn^{2+} replaces Co^{2+}. Go through the literatures, the experimental value of Co_3O_4 $\approx$1.5−1.6 eV [39], and the calculated band gap energy of the Co_3O_4 are

1.1026 [40] and 1.8 eV [41], respectively. Our result (1.357 eV) is in good agreement with the experimental value. Figures 2d (blue and yellow regions indicating electron increase and decrease, respectively) explained the reason of the increased band gap. The electron accepting ability of Zn^{2+} is weaker than that of Co^{2+} and Zn^{2+} at the tetrahedral sites (8a) in the spinel structure weakens the electron accepting ability of $ZnCo_2O_4$. This is further confirmed by the corresponding densities of states (DOS). The total DOS reveal that the spinel Co_3O_4 (Figure S1b) has less DOS near the Fermi level than the spinel $ZnCo_2O_4$ (Figure 2b). According to quantum theory, only electrons near the Fermi level can contribute to the current under an external electric field and the electrical conductivity is proportional to the electrons at the Fermi level [42]. The electron effective mass of Co_3O_4 and $ZnCo_2O_4$ were compared by a simple method. Figure S2 shows the band structures of the two materials, and it is found that the energy bands of $ZnCo_2O_4$ are more flatter than that of Co_3O_4 near the Fermi level. This means the former has the larger electron effective mass, and further illustrates the $ZnCo_2O_4$ has lower band mobility compared with Co_3O_4. Hence, the conductivity of $ZnCo_2O_4$ is a slightly less than that of Co_3O_4 as a result of the change in the band structure. The electrical resistivity of Co_3O_4 and $ZnCo_2O_4$ were also measured by four-point probe method. The square resistance of Co_3O_4 is 52 kΩ/sqr and thickness is about 0.2 mm, so the electrical resistivity of the Co_3O_4 is about 1040 Ω cm, which is in good agreement with the previous report [43]. Under the same experimental conditions, the electrical resistivity of $ZnCo_2O_4$ is an order of magnitude higher than Co_3O_4. However, in practice, the small change is tolerable if benefits such as eco-friendliness (low toxicity) and low cost are considered. These satisfactory results evaluated the rationality of the experimental scheme. The calculation also indicates that the magnetic properties of the spinel structure disappear after Zn^{2+} substitutes Co^{2+}.

The X-ray diffraction (XRD) pattern in Figure 3a that can be indexed to the cubic spinel structure of $ZnCo_2O_4$ (JCPDS No. 23-1390) [44] shows the dominant (311) peaks revealing the preferred (311) orientation. The characteristic peaks of laser Raman spectrograms in Figure 3b and XPS spectra in Figure 3c~f disclose the presence of Zn, Co and O suggesting the formation of $ZnCo_2O_4$.

Figures 4d and Figures 5d schematically illustrates the formation mechanism of $ZnCo_2O_4$ nanoflowers ($ZnCo_2O_4$ NFs) and $ZnCo_2O_4$ nanowires ($ZnCo_2O_4$ NWs), respectively. Nickel plated metal fibers and carbon fibers are flexible and conductive rendering them excellent substrates to fabricate nanostructured $ZnCo_2O_4$ hydrothermally according to the following reactions (1-4): [45]

$$H_2NCONH_2 + H_2O \rightarrow 2NH_3 + CO_2 \qquad (1)$$

$$CO_2 + H_2O \rightarrow CO_3^{2-} + 2H^+ \qquad (2)$$

$$NH_3 + H_2O \rightarrow NH_4^+ + OH^- \qquad (3)$$

$$2/3\ Co^{2+} + 1/3\ Zn^{2+} + OH^- + 1/2\ CO_3^{2-} + n\ H_2O \rightarrow Zn_{1/3}Co_{2/3}(OH)(CO_3)_{1/2}nH_2O \qquad (4)$$

Annealing at 400 °C (ramping rate of 2 °C min^{-1}) converts the precursors into spinel $ZnCo_2O_4$ NFs and $ZnCo_2O_4$ NWs as follows:

$$6\ Zn_{1/3}Co_{2/3}(OH)(CO_3)_{1/2}nH_2O + O_2 \rightarrow 2\ ZnCo_2O_4\uparrow + 3CO_2\uparrow + (6n+3)\ H_2O \qquad (5)$$

The formation involves two steps. Firstly, the $ZnCo_2O_4$ NFs and $ZnCo_2O_4$ NWs precursors self-assemble under hydrothermal conditions. At the proper pH controlled by the mass of urea and hydrolysis producing OH^- and CO_3^{2-} at a high temperature and high pressure, Zn^{2+} and Co^{2+} combine with OH^- and CO_3^{2-} in the solution and post-annealing in air produces to form the $ZnCo_2O_4$ NFs and $ZnCo_2O_4$ NWs on the substrate.

SEM images disclose that $ZnCo_2O_4$ NFs and $ZnCo_2O_4$ NWs are produced with high yields. The optical images of the $ZnCo_2O_4$ NFs and $ZnCo_2O_4$ NWs are depicted in Figure S3 and the color contrast indicates the materials were fabricated successfully. Figure S4 presents the SEM images of the conductive and flexible substrates, nickel plated metal fibers (Figures S4a and 4b) and carbon fibers (Figures S4c and 4d). The surface of the carbon fibers is smooth prior to the $ZnCo_2O_4$ NWs growth and the particles on the metal fibers maybe generated by nickel plating. Figure 4a-c displays the SEM images of $ZnCo_2O_4$ NFs at low, medium and high magnifications with an average diameter of 8 μm (Figure 4a). Figure S5 shows large areas of the flower-like $ZnCo_2O_4$. The higher-magnification SEM images in Figures 4c show that the $ZnCo_2O_4$ NFs are comprises of many nanosheets which consisting of a large number of nanoparticles. These nanosheets are interconnected and grow radially from the center forming the flower-like structure. This unique morphology improves the electron transport between the nanosheets and improves the durability of the structure during the fast redox reaction. Undoubtedly, these advantages may enhance the electrochemical performance. Figure 5a-c depicts the SEM images of the $ZnCo_2O_4$ NWs at different magnifications indicating the as prepared nanowires arrays growth on the carbon fibers were large-area and uniform. Figures 5a and 5b disclose retention of the 3D structure of the carbon fibers which are covered by $ZnCo_2O_4$ NWs uniformly. Examination of an individual carbon fiber reveals that the $ZnCo_2O_4$ NWs grow orderly and closely on the carbon fibers with a large aspect ratio (Figures 5c). After ultrasonic treatment for several minutes, the $ZnCo_2O_4$ NWs are examined by FE-SEM which shows that the nanowires adhere well on the carbon fibers. The high-magnification SEM images in Figures 4c and Figures 5c show that the $ZnCo_2O_4$ NFs and $ZnCo_2O_4$ NWs have porous structures due to gas release during decomposition of the precursors. The Brunauer–Emmet–Teller (BET) surface areas of $ZnCo_2O_4$ NWs was calculated to be 59.386 m^2 g^{-1}, and average pore width is about 50 nm. The large surface area is expected to yield a high specific capacitance due to the easy access of the active materials to the interface in the redox process. The TEM images of the $ZnCo_2O_4$ NFs and $ZnCo_2O_4$ NWs in Figure 6 confirm that the porous structure consisting of many nanoparticles. The lattice spacing of 0.24 nm shown in Figures 6b and 6e corresponds to the (311) planes of spinel $ZnCo_2O_4$ and the circular SAED patterns of the $ZnCo_2O_4$ NFs (inset in Figure 6b) and $ZnCo_2O_4$ NWs (inset of Figure 6e) indicate a polycrystalline nature.

To evaluate the electrochemical performance of the synthesized nanostructures, electrochemical measurements were performed by a three-electrode system with 2 M KOH aqueous electrolyte, a platinum foil counter electrode and an Ag/AgCl reference electrode. The CV curves of $ZnCo_2O_4$ NFs and $ZnCo_2O_4$ NWs electrodes at various scan rates with a potential windows ranging from 0 to 0.8 V (vs. Ag/AgCl) are presented in Figure 7a and 7d. The shapes of these CV curves remained virtually unchanged with the potential scan rates varied from 2 to 50 mV s^{-1}, revealing the ideal capacitive behaviors and good rate capabilities of the $ZnCo_2O_4$ NFs and $ZnCo_2O_4$ NWs electrodes. The shape of the CV curves clearly reveals the pseudocapacitive characteristics. Specifically, a pair of redox peaks can be observed within the potential range from 0 to 0.8 V (vs. Ag/AgCl) for all sweep rates, which is mainly related to the faradic redox reactions in the alkaline electrolyte. With the scan rates increase, the cathodic peak position shifts to lower potential, which is attributed to the polarization effect. Figure 7b and 7e illustrates that the galvanostatic charge-discharge (GCD) curves of $ZnCo_2O_4$ NFs and $ZnCo_2O_4$ NWs electrodes measured in the current densities from 2 to 10 A g^{-1}. These charging and discharging curves of the ternary electrodes are highly symmetric, arising from the ideal capacitance behavior and fast Faraday reaction. Figure 7c and 7f schematically illustrates the kinetic advantages of the hybrid structures in electrochemical energy storage. As shown in Figure 4c, the nanoflowers are comprises of many porous nanosheets and these nanosheets interconnected with each other, not only this unique structure improves the electron transport between the nanosheets and improves the durability of the structure during the fast redox reaction. Analogous, one dimensional porous nanowires structure provides an excellent electronic transmission path in electrochemical reaction. Moreover, the speed of the electronic transmission was further accelerated due to the flexible and conductive substrates. Without question, these advantages could enhance the electrochemical performance.

To further explore the practical applications of this design, an all-solid-state symmetric SCs was assembled using the $ZnCo_2O_4$ NFs and $ZnCo_2O_4$ NWs as the electrodes with the Polyvinyl alcohol (PVA)/KOH as gel electrolyte (denoted as $ZnCo_2O_4$ NFs//$ZnCo_2O_4$ NWs). In contrast to liquid-based SCs, solid-state device has several advantages such as flexibility, ease of fabrication, large working temperature and improved safety. Figures 8a and 8b show the photographs of the small and flexible device and Figure 8c schematically illustrates the structure. The PVA/KOH gel serves as the electrolyte and separator simultaneously in this device thus simplifying the assembly process. Figure 8d displays the CV curves of the device at different voltages at a scanning rate of 10 mV s^{-1}. The curves are stable even at 1.4 V indicating good capacitive behavior. Figure 8e shows the CV curves acquired at scanning rates of 5, 10, 20, 50, and 100 mV s^{-1} in a voltage window of between 0 and 1.4 V. The CV profiles are stable as the scanning rate increases from 5 to 100 mV s^{-1} revealing fast charging and discharging characteristics. The GCD curves obtained at different current densities are presented in Figure 8f. The discharge curves are almost symmetrical to the charge curves, indicating good capacitive behavior for the device. The corresponding specific capacitance plotted in Figure 9a were derived by the following equation:

$$C = (I \times \Delta t) / (m \times \Delta V) \qquad (6)$$

Where I (A) is the constant discharge current and m(g), Δt (s), and ΔV (V) designate the mass of active materials, discharging time, and potential drop during discharging, respectively. The total mass of active materials is approximately 20 mg. The device show capacitances of 220.6, 167.6, 148, 116.6 and 87.14 F g^{-1} at current density of 2, 3, 4, 6, and 10 A g^{-1}, respectively. Figure 9b shows the cycling performance at a current density of 2 A g^{-1} for up to 8,000 cycles and retention of 67.5%. The degradation in the capacitance stems from destruction of the electrode by the harsh redox reactions and the consumption of gel electrolyte caused by an irreversible reaction between the electrode material and electrolyte. As illustrated inset of Figure 9b, the $ZnCo_2O_4$ NFs and $ZnCo_2O_4$ NWs structures were well maintained and overall preserved with little structural deformation after 8000 cycles. The intrinsic electrochemical and kinetic mechanism of the electrodes ware analyzed by the EIS studies. Figure 9c illustrates the Nyquist plots of EIS spectra of $ZnCo_2O_4$ NFs, $ZnCo_2O_4$ NWs and the device in the frequency range from 10 kHz to 0.01 Hz. In the low-frequency area, the inclined line represents the Warburg (W) impedance corresponding to the electrolyte diffusion in porous electrode and proton diffusion in host materials. The $ZnCo_2O_4$ NWs electrode has the largest slope in all electrodes, indicating its best capacitive performance with lower diffusion resistance. This can be attributed to the nanowires separate with each other and thus facilitates the flowing of the electrolyte. In high frequency area, the intercept to x axis represents the bulk resistance of the electrochemical system (Re), and the semicircle corresponds to the parallel combination of double-layer capacitance (CPE) and charge transfer resistance (Rct) at the working electrode-electrolyte interface. Compared to the other electrodes, $ZnCo_2O_4$ NWs has a smaller Re, due to the carbon fibers substrate increases the electrical conductivity.

To evaluate the flexibility and stability of the device, the circulation properties are assessed at different bending angles of 0 (without bending), 60, 90, and 120 degrees. The influence of the bending-induced mechanical stress upon the specific capacitance is illustrated in Figure 9d which shows negligible capacitance change even though the device is bent substantially. The Ragone plot describing the relationship between the energy and power densities is shown in Figure 9e with data obtained from traditional lithium ion batteries (LIBs) and EDLC provided for comparison. The energy and power densities (E and P) are calculated by the following equations:

$$E = (C \times \Delta V^2)/2 \tag{7}$$

$$P = E/\Delta t \tag{8}$$

Where, C (F g^{-1}) is the specific capacitance of the device. The maximum energy density of 60.04 Wh kg^{-1} at a power density of 1.4 KW kg^{-1} and power density of 7

KW kg^{-1} at an energy density of 23.72 Wh kg^{-1} are achieved at an operating voltage of 1.4 V, which are better than the energy and power densities achieved previously from $ZnCo_2O_4$@MnO_2//a-Fe_2O_3 (energy density 37.8 W h kg^{-1} at a power density of 648 W kg^{-1}) [46], $NiCo_2O_4$@MnO_2//AC (energy density 35 W h kg^{-1} at a power density of 163 W kg^{-1}) [47], NiO//carbon (15 W h kg^{-1} at a power density of 447 Wkg^{-1}) [48].

In order to explore the potential application of $ZnCo_2O_4$ NFs//$ZnCo_2O_4$ NWs device as a flexible power source, we further demonstrate the practical application of the device by powering a light-emitting diode (LED). As shown in the insets in Figure 9f, the two devices connected in series can power three 3 mm diameter red LED [1.8 V, 20 mA] for more than 10 min (strong light) and they are effective even for 30 min.

4. Conclusion

A low-cost and large-area technique to produce eco-friendly $ZnCo_2O_4$ NFs and $ZnCo_2O_4$ NWs is designed and described. The high electrochemical activity and stability of the $ZnCo_2O_4$ NFs//$ZnCo_2O_4$ NWs symmetrical device suggest large potential of $ZnCo_2O_4$ in energy storage. Theoretical assessment confirms the rationality of the experimental scheme and explains the increased band gap. The device shows superior capacity of 220.6 F g^{-1} at a current density of 2 A g^{-1} as well as long-term cycling stability with 67.5% capacitance retention after 8,000 cycles. The maximum energy density of 60.04 Wh kg^{-1} at a power density of 1.4 KW kg^{-1} and power density of 7 KW kg^{-1} at an energy density of 23.72 Wh kg^{-1} are accomplished at an operating voltage of 1.4 V. The excellent properties, stability, and durability bode well for commercial adoption of the nanostructured $ZnCo_2O_4$ materials in future high-performance SCs.

Acknowledgments

This work was jointly supported by the Fundamental Research Funds for the Central Universities (53200959770), Special Construction project of Beijing city Education Committee (519002650733), and City University of Hong Kong Applied Research Grant (ARG) No. 9667104.

Notes and references

[1] P. Simon, Y. Gogotsi, Nat. Mater., 2008, **7**, 845-854.

[2] M. S. Dresselhaus, I. L. Thomas, Nature, 2011, **414**, 332-337.

[3]D. Y. Zhang, Y. H. Zhang, Y. S. Luo, P. K. Chu, Nano Energy, 2015, **13**, 45-47.

[4] Y. S. Luo, J. S. Luo, J. Jiang, W. W. Zhou, H. P. Yang, X. Y. Qi, H. Zhang, H. J. Fan, Y. W. Y. Denis, C. M. Li, T. Yu, Energ. Environ. Sci., 2012, **5**, 6559-6566.

[5] Z. Y. Zhang, F. Xiao, L. H. Qian, J. W. Xiao, S. Wang, Y. Q. Liu, Adv. Energy Mater., 2014, **4**, 1400064-100073.

[6] W. M. Du, X. Han, L. Lin, M. X. Chen, X. Y. Li, C. F. Pan, Z. L. Wang, Adv. Energy Mater., 2014, **4**, 1301592-1301797.

[7]C. F. Pan, L. Dong, G. Zhu, S. Niu, R. M. Yu, Q. Yang, Y. Liu, Z. L. Wang, Nat. Photonics, 2013, **7**, 752-758.

[8] Z. N. Yu, M. McInnis, J. Calderon, S. Seal, J. Thomas, Nano Energy, 2015, **11**, 611-620.

[9] D. Y. Zhang, H. L. Yan, Y. Lu, K. W. Qiu, C. L. Wang, Y. H. Zhang, X. M. Liu, J. S. Luo, Y. S. Luo, Dalton Trans., 2014,**43**, 15887-15897.

[10] D. Y. Zhang, H. L. Yan, Y. Lu, K. W. Qiu, C. L. Wang, C. C. Tang, Y. H. Zhang, C. W. Cheng, Y. S. Luo, Nanoscale Res. Lett., 2013, **9**, 139-147.

[11] Y. P. Fu, X. Cai, H. W. Wu, Z. B. Lv, S. C. Hou, M. Peng, X. Yu, D. C. Zou, Adv. Mater., 2012, **24**, 5713-5718.

[12] Z. N. Yu, L. Tetard, L. Zhai, J. Thomas, Energ. Environ. Sci., 2015, **8**, 702-730.

[13] F. Meng, Y. Ding, Adv. Mater., 2011, **23**, 4098-4102.

[14] K. Wang, W. Zou, B. Quan, A. Yu, H. Wu, P. Jiang, Z. Wei, Adv. Energy Mater., 2011, **1**, 1068.

[15] M. Kaempgen, C.K. Chan, J. Ma, Y. Cui, G. Gruner, Nano Lett., 2009, **9**, 1872-1876.

[16] A.S. Arico, P. Bruce, B. Scrosati, J.M. Tarascon, W. V. Schalkwijk, Nat. Mater., 2005, **4**, 366-377.

[17] P. Simon, Y. Gogotsi, B. Dunn, Science Magazine, 2014, **343**, 1210-1211.

[18] Z. N. Yu, J. Thomas, Adv. Mater., 2014, **26**, 4279-4285.

[19] H. Y. Wang, F. X. Xiao, L. Yu, B. Liu, X. W. (David) Lou, Small, 2014, **10**, 3181-3186.

[20]L. F. Shen, Q. Che, H. S. Li, X. G. Zhang, Adv. Funct. Mater., 2014, **24**, 2736-2736.

[21]K. Jost, C. R. Perez, J. K. McDonough, V. Presser, M. Heon, G. Dion Y. Gogotsi, Energ. Environ. Sci., 2011, **4**, 5060-5067.

[22] M. V. Reddy, G. V. Subba Rao, B. V. R. Chowdari, Chem. Rev., 2013, **113**, 5364-5457.

[23] J. P. Liu, J. Jiang, C. W. Cheng, H. X. Li, J. X. Zhang, H. Gong, H. J. Fan, Adv. Mater., 2011, **23**, 2076-2081.

[24] Y. S. Luo, J. Jiang, W. W. Zhou, H. P. Yang, J. S. Luo, X. Y. Qi, H. Zhang, D. Y. W. Yu, C. M. Li, T. Yu, J. Mater. Chem., 2012, **22**, 8634-8640.

[25] L. F. Hu, L.M. Wu, M.Y. Liao, X. H. Hu, X. S. Fang, L. Hu, L. Wu, M. Liao, Adv. Funct. Mater., 2012, **22**, 998-1004.

[26] Y. S. Luo, J. S. Luo, W. W. Zhou, X. Y. Qi, H. Zhang, Y. W. Y. Denis, C. M. Li, H. J. Fan, T. Yu, J. Mater. Chem. A., 2013, **1**, 273-281.

[27] C. Zhou, Y. W. Zhang, Y. Y. Li, J. P. Liu, Nano Lett., 2013, **13**, 2078-2085.

[28] J. S. Luo, X. H. Xia, Y. S. Luo, C. Guan, J. L. Liu, X. Y. Qi, C. F. Ng, T. Yu, H. Zhang, H. J. Fan, Adv. Energy Mater., 2013, **3**, 737-743.

[29] J. S. Luo, J. L. Liu, Z. Y. Zeng, C. F. Ng, L. J. Ma, H. Zhang, J. Y. Lin, Z. X. Shen, H. J. Fan Nano Lett., 2013, **13**, 6136-6143.

[30] W. Luo, X. L. Hu, Y. M. Sun, Y. H. Huang, J. Mater. Chem., 2012, **22**, 8916-8921.

[31] W. W. Zhou, J. P. Liu, T. Chen, K. S. Tan, X. T. Jia, Z. Q. Luo, C. X. Cong, H. P. Yang, C. M. Li, T. Yu, Phys. Chem. Chem. Phys., 2011,**13**, 14462-14465.

[32] Q. C.Liu, J. J. Xu, Z. W. Chang. X. B. Zhang, J. Mater. Chem. A, 2014, **2**, 6081-6085.

[33] B. Liu, B. Y. Liu , Q. F. Wang , X. F. Wang, Q. Y. Xiang, D. Chen, G. Z. Shen, ACS Appl. Mater. Interfaces, 2013, **5**, 10011-10017.

[34] K. W. Qiu, Y. Lu, D. Y. Zhang, J. B. Cheng, H. L. Yan, J. Y. Xu, X. M. Liu, J. K. Kim, Y. S. Luo, Nano Energy, 2015, **11**, 687-696.

[35] A. C. Siegel, S. T. Phillips, M. D. Dickey, N. Lu, Z. Suo, G. M. Whitesides, Adv. Funct. Mater., 2010, **20**, 28-35.

[36] A. W. Martinez, S. T. Phillips, M. J. Butte and G. M. Whitesides, Angew. Chem. Int. Ed., 2007, **46**, 1318-1320.

[37] F. C. Krebs, T. Tromholt, M. Jorgensen, Nanoscale, 2010, **2**, 873-886.

[38] S. J. Clark, M. D. Segall, C. J. Pickard, P. J. Hasnip, M. J. Probert, K. Refson, M. C. Payne, Zeitschrift für Kristallographie, 2005, **220**, 567-570.

[39] J. van Elp, J. L. Wieland, H. Eskes, P. Kuiper, G. A. Sawatzky, F. M. F. de Groot, T. S. Turner, Phys. Rev. B, 1991, **44**, 6090-6103.

[40] Y. R. Zhu, X. B. Ji, Z. P. Wu, W. X. Song, H. S. Hou, Z. B. Wu, X. He, Q. Y. Chen, C. E. Banks, J. Power Sources, 2014, **267**, 888-900.

[41] Y. C. Wang, T. Zhou, K. Jiang, P. M. Da , Z. Peng, J. Tang, B. Kong, W. B. Cai, Z. Q. Yang, G. F. Zheng, Adv. Energy Mater., DOI: 10.1002/aenm.201400696.

[42] U. Mizutani, Introduction to the Electron Theory of Metals, Cambridge University Press, United Kingdom, 2001.

[43] V. R. Shinde, S. B. Mahadik, T. P. Gujar, C. D. Lokhande, Appl. Surf. Sci., 2006, **252**, 7487-7492.

[44] N. C. Li, C. R. Martin and B. Scrosati, J. Power Sources, 2001, **97**, 240-243.

[45] H. X. Chen, Q. B. Zhang, J. X. Wang, Q. Wang, X. Zhou, X. H. Li, Y. Yang, K. L. Zhang, Nano Energy, 2014, **10**, 245-258.

[46] W. Q. Ma, H. H. Nan, Z. X. Gu, B. Y. Geng, X. J. Zhang, J. Mater. Chem., A 2015, **3**, 5442-5448.

[47] Z. S. Wu, W. C. Ren, D. W. Wang, F. Li, B. L. Liu, H. M. Cheng, ACS Nano, 2010, **4**, 5835-5842.

[48] X. Lu, M. Yu, T. Zhai, G. Wang, S. Xie, T. Liu, C. Liang, Y. Tong, Y. Li, Nano Lett., 2013, **13**, 2628-2633.

Figure captions

Figure 1. (a-c) Crystal structure of spinel Co_3O_4; (d-f) crystal structure of spinel $ZnCo_2O_4$; (g-i) CoO_6 octahedron, CoO_4 tetrahedron, and ZnO_4 tetrahedron, respectively. Znions occupy the tetrahedral sites and Coions occupy the octahedral sites.

Figure 2. (a) Calculated band structure; (b) Total densities of states; (d) electron density difference by the CASTEP for the spinel $ZnCo_2O_4$ (the blue and yellow regions indicate electron increase and decrease, respectively). (c) (1 0 0) crystal face of spinel $ZnCo_2O_4$.

Figure 3. Properties of the as prepared spinel $ZnCo_2O_4$ nanomaterials. (a) XRD patterns of $ZnCo_2O_4$ NFs and NWs; (b) Raman spectra of $ZnCo_2O_4$ NFs and NWs; (c) XPS general spectrum of spinel $ZnCo_2O_4$; (d-f) Corresponding Co 2p, Zn 2p, and O 1s XPS peaks.

Figure 4. Morphologies and schematic diagram for the formation mechanism of the 3D $ZnCo_2O_4$ NFs. (a, b) low-magnification and enlarged SEM images of $ZnCo_2O_4$ NFs; (c) high-magnification SEM image of $ZnCo_2O_4$ NFs; (d) proposed mechanism for the fabrication of $ZnCo_2O_4$ NFs by the self-assembly process.

Figure 5. Morphologies and schematic diagram for the formation mechanism of the $ZnCo_2O_4$ NWs arrays. (a, b) low-magnification and enlarged SEM images of $ZnCo_2O_4$ NWs; (c) high-magnification SEM image of $ZnCo_2O_4$ NWs; (d) proposed mechanism for the fabrication of $ZnCo_2O_4$ NWs arrays by the self-assembly process.

Figure 6. (a, b) Low-magnification and high-magnification TEM images of the $ZnCo_2O_4$ NFs; (c-e) low-magnification and high-magnification TEM images of the $ZnCo_2O_4$ NWs. The insets of (b) and (e) are the corresponding SAED patterns obtained from the $ZnCo_2O_4$ NFs and $ZnCo_2O_4$ NWs.

Figure 7. Electrochemical properties of the $ZnCo_2O_4$ nanomaterials under three-electrode measurement system. (a) and (d) CV curves of the $ZnCo_2O_4$ NFs and $ZnCo_2O_4$ NWs at the different scan rates; (b) and (e) discharging curves of the $ZnCo_2O_4$ NFs and $ZnCo_2O_4$ NWs at different current densities; (c) and (f) schematic diagrams showing the kinetic advantages of the $ZnCo_2O_4$ NFs and $ZnCo_2O_4$ NWs in electrochemical energy storage.

Figure 8. (a, b) Photographs of the device; (c) schematic illustration of the structure of the all-solid-state device; (d) CV curves acquired at different voltages at a scanning rate of 10 mV s^{-1}; (e) CV curves measured at scanning rates of 5, 10, 20, 50, and 100 mV s^{-1}at voltages between 0 and 1.4 V; (f) GCD curves of the device at different current densities.

Figure 9. (a) Calculated specific capacities; (b) cycling performance of the device at a current density of 2 A g^{-1} for 8,000 cycles; (c) electrochemical impedance spectra (EIS) of the $ZnCo_2O_4$ NWs, $ZnCo_2O_4$ NFs and $ZnCo_2O_4$ NFs //$ZnCo_2O_4$ NWs electrodes; (d) Influence of the bending-induced mechanical stress upon specific capacitance; (e) Ragone plots of the device in comparison with other recently reported values from SCs; (f) optical images of three red LEDs powered by two all solid-state SCs connected in series.

Figure

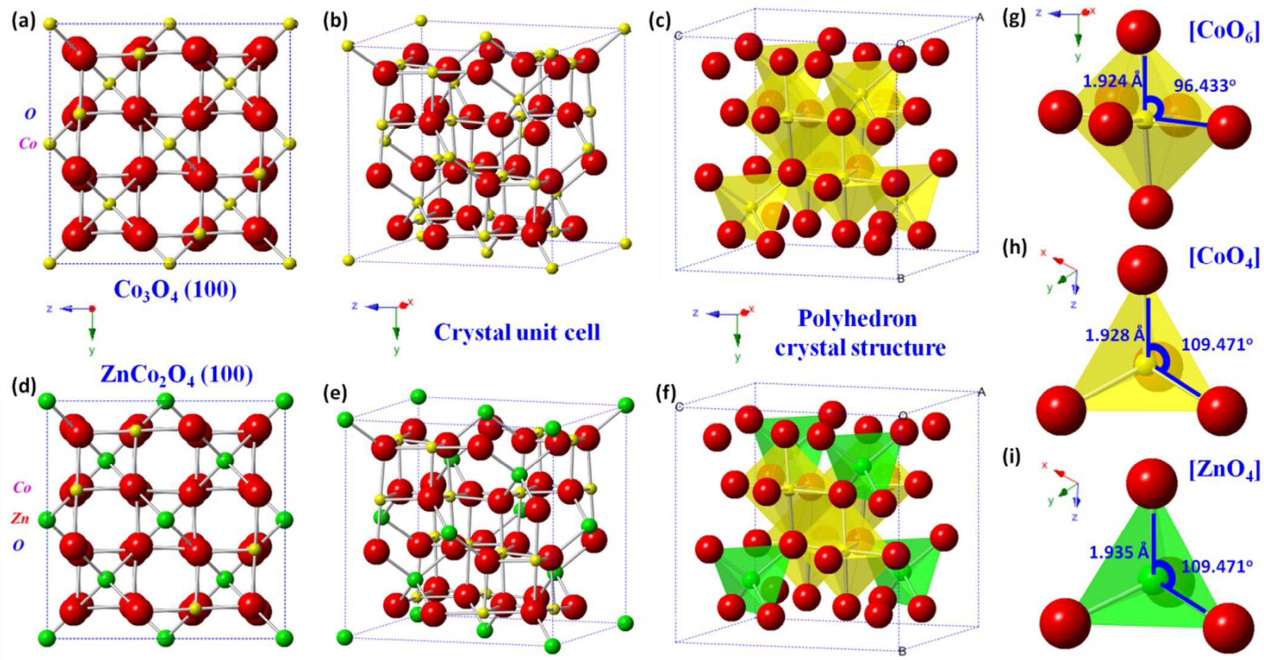

Figure 1. (a-c) Crystal structure of spinel Co_3O_4; (d-f) crystal structure of spinel $ZnCo_2O_4$; (g-i) CoO_6 octahedron, CoO_4 tetrahedron, and ZnO_4 tetrahedron, respectively. Znions occupy the tetrahedral sites and Coions occupy the octahedral sites.

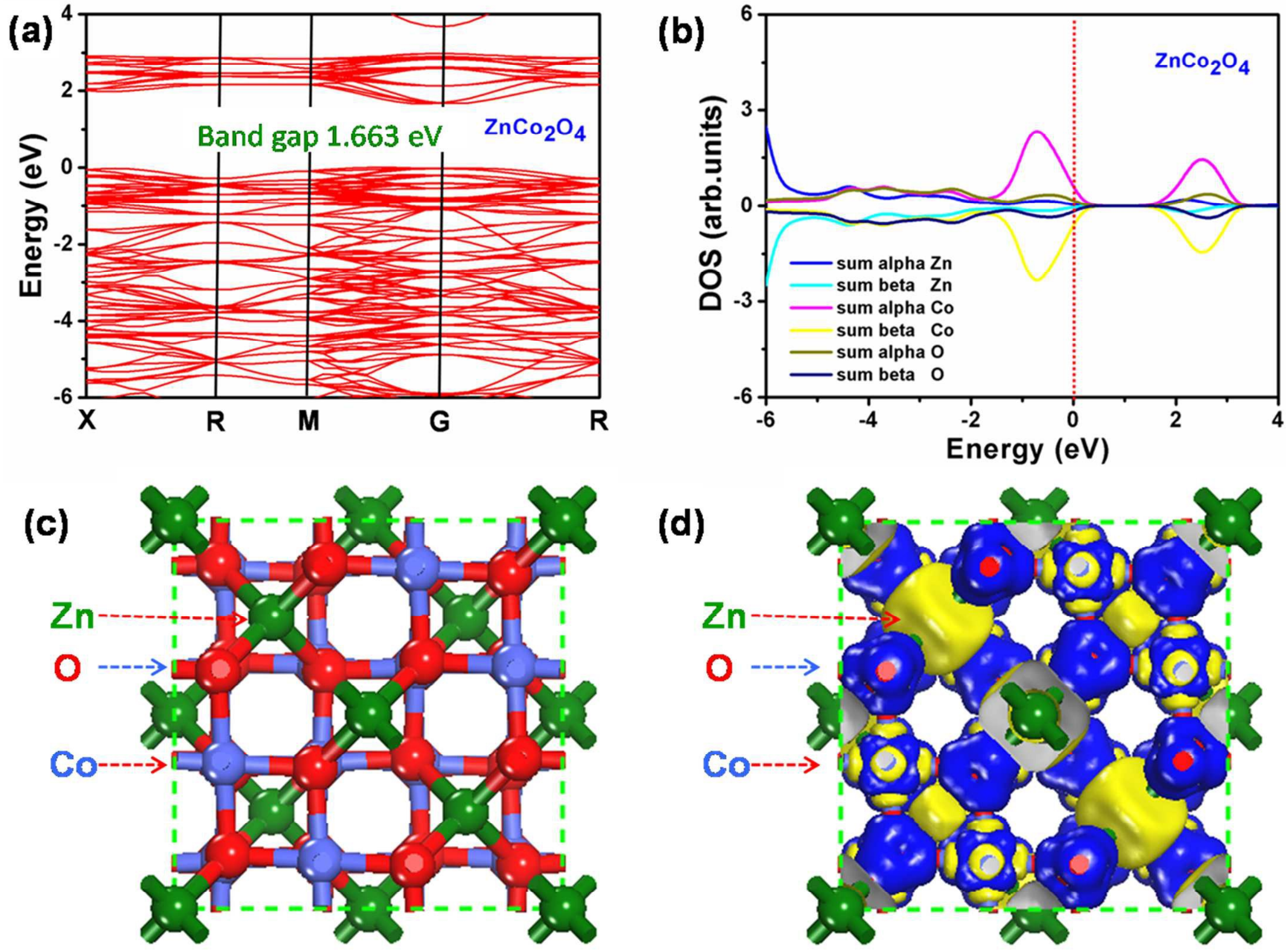

Figure 2. (a) Calculated band structure; (b) Total densities of states; (d) electron density difference by the CASTEP for the spinel $ZnCo_2O_4$ (the blue and yellow regions indicate electron increase and decrease, respectively). (c) (1 0 0) crystal face of spinel $ZnCo_2O_4$.

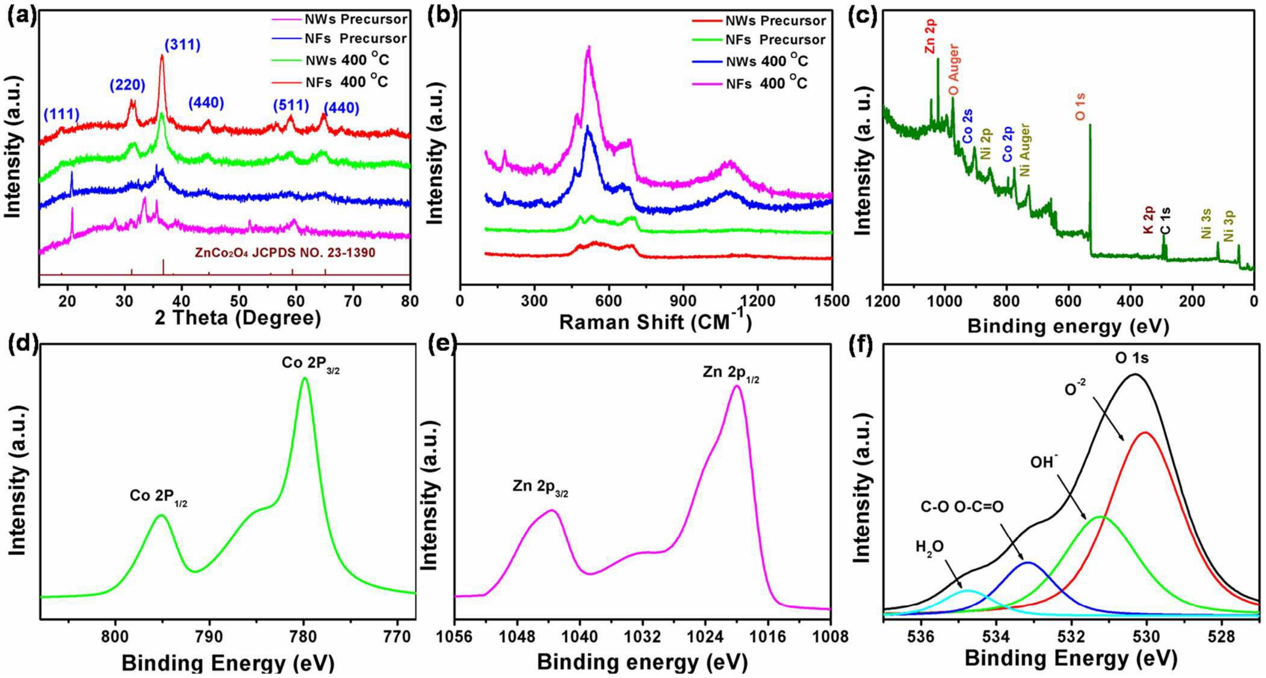

Figure 3. Properties of the as prepared spinel $ZnCo_2O_4$ nanomaterials. (a) XRD patterns of $ZnCo_2O_4$ NFs and NWs; (b) Raman spectra of $ZnCo_2O_4$ NFs and NWs; (c) XPS general spectrum of spinel $ZnCo_2O_4$; (d-f) Corresponding Co 2p, Zn 2p, and O 1s XPS peaks.

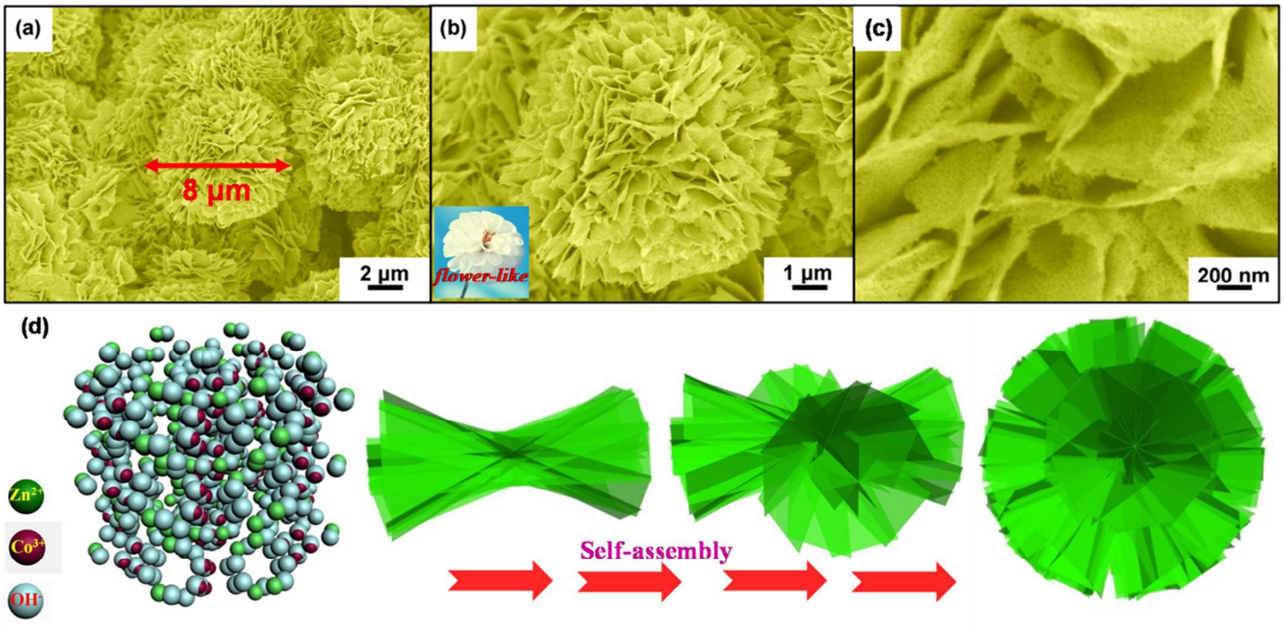

Figure 4. Morphologies and schematic diagram for the formation mechanism of the 3D $ZnCo_2O_4$ NFs. (a, b) low-magnification and enlarged SEM images of $ZnCo_2O_4$ NFs; (c) high-magnification SEM image of $ZnCo_2O_4$ NFs; (d) proposed mechanism for the fabrication of $ZnCo_2O_4$ NFs by the self-assembly process.

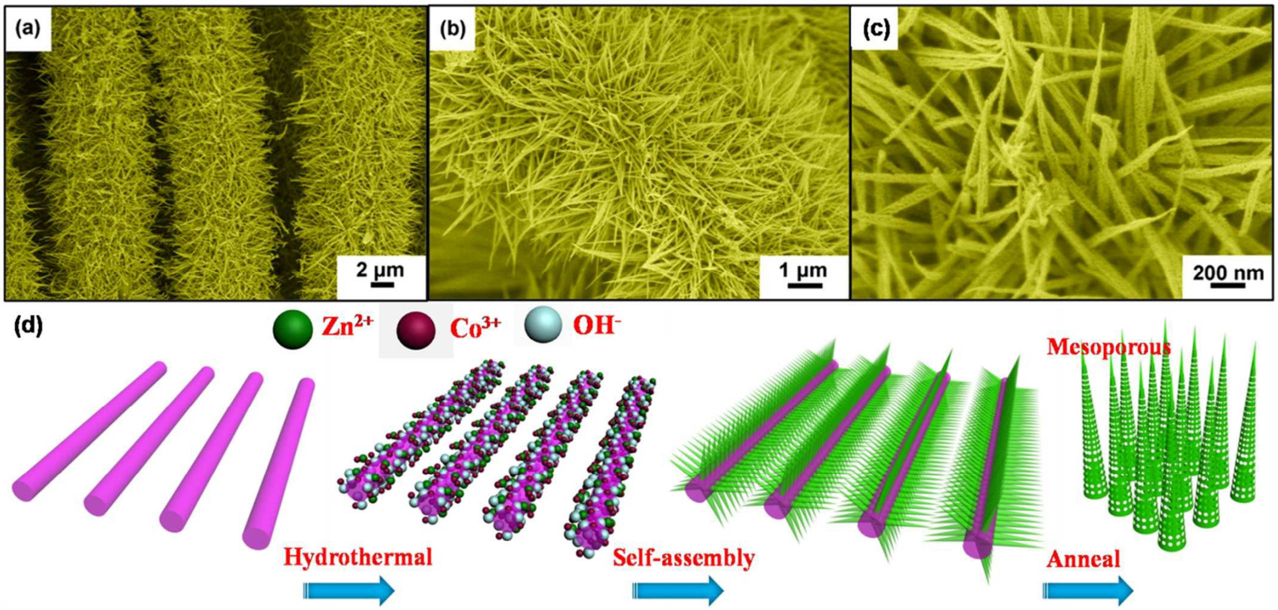

Figure 5. Morphologies and schematic diagram for the formation mechanism of the $ZnCo_2O_4$ NWs arrays. (a, b) low-magnification and enlarged SEM images of $ZnCo_2O_4$ NWs; (c) high-magnification SEM image of $ZnCo_2O_4$ NWs; (d) proposed mechanism for the fabrication of $ZnCo_2O_4$ NWs arrays by the self-assembly process.

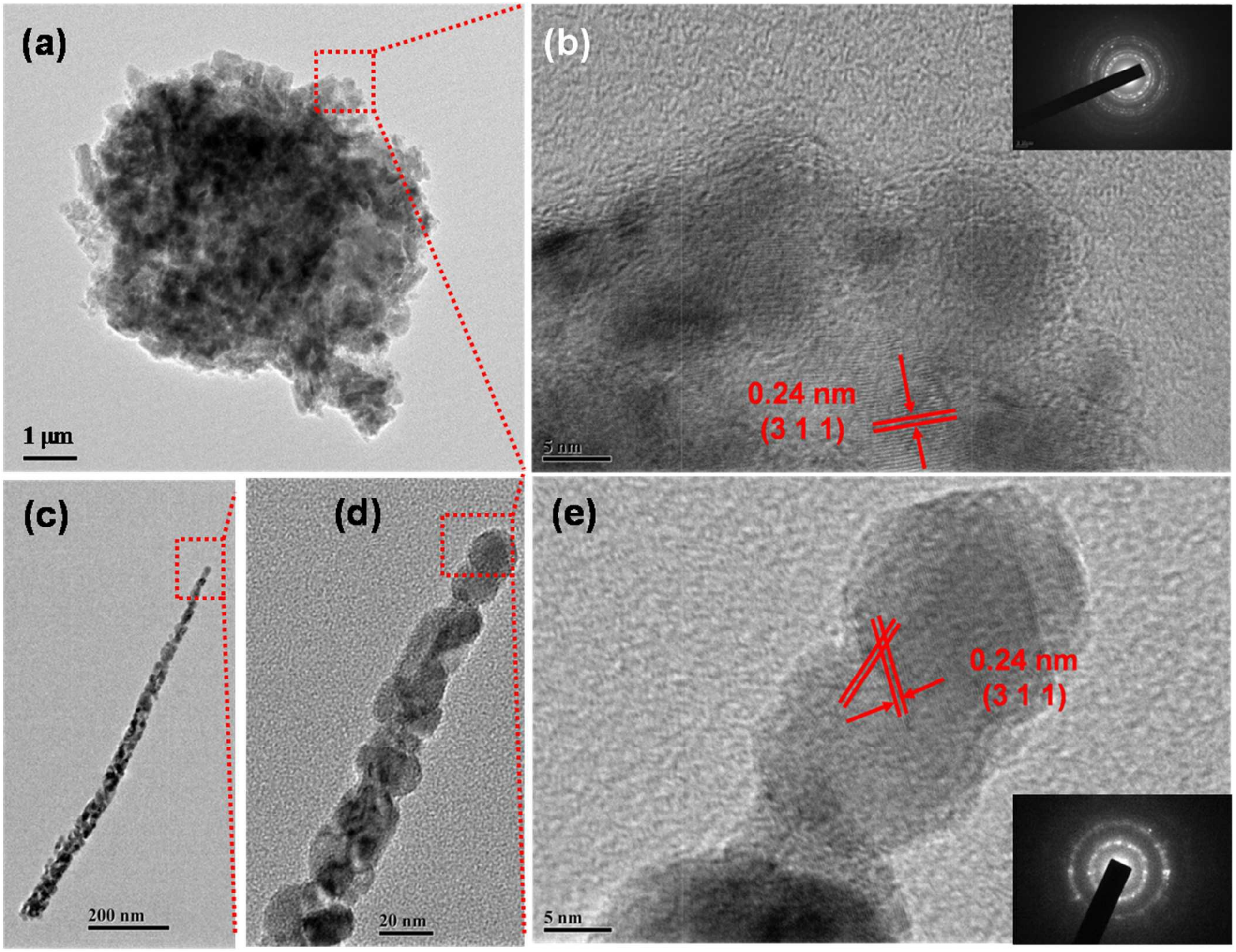

Figure 6. (a, b) Low-magnification and high-magnification TEM images of the $ZnCo_2O_4$ NFs; (c-e) low-magnification and high-magnification TEM images of the $ZnCo_2O_4$ NWs. The insets of (b) and (e) are the corresponding SAED patterns obtained from the $ZnCo_2O_4$ NFs and $ZnCo_2O_4$ NWs.

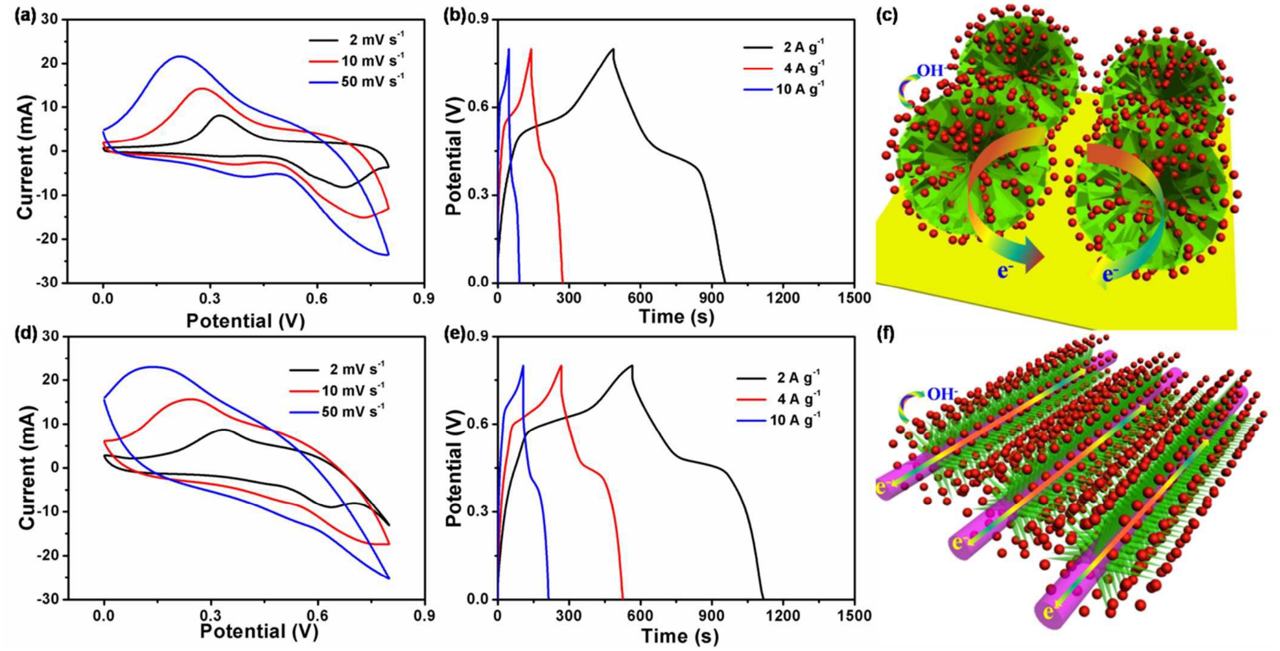

Figure 7. Electrochemical properties of the $ZnCo_2O_4$ nanomaterials under three-electrode measurement system. (a) and (d) CV curves of the $ZnCo_2O_4$ NFs and $ZnCo_2O_4$ NWs at the different scan rates; (b) and (e) discharging curves of the $ZnCo_2O_4$ NFs and $ZnCo_2O_4$ NWs at different current densities; (c) and (f) schematic diagrams showing the kinetic advantages of the $ZnCo_2O_4$ NFs and $ZnCo_2O_4$ NWs in electrochemical energy storage.

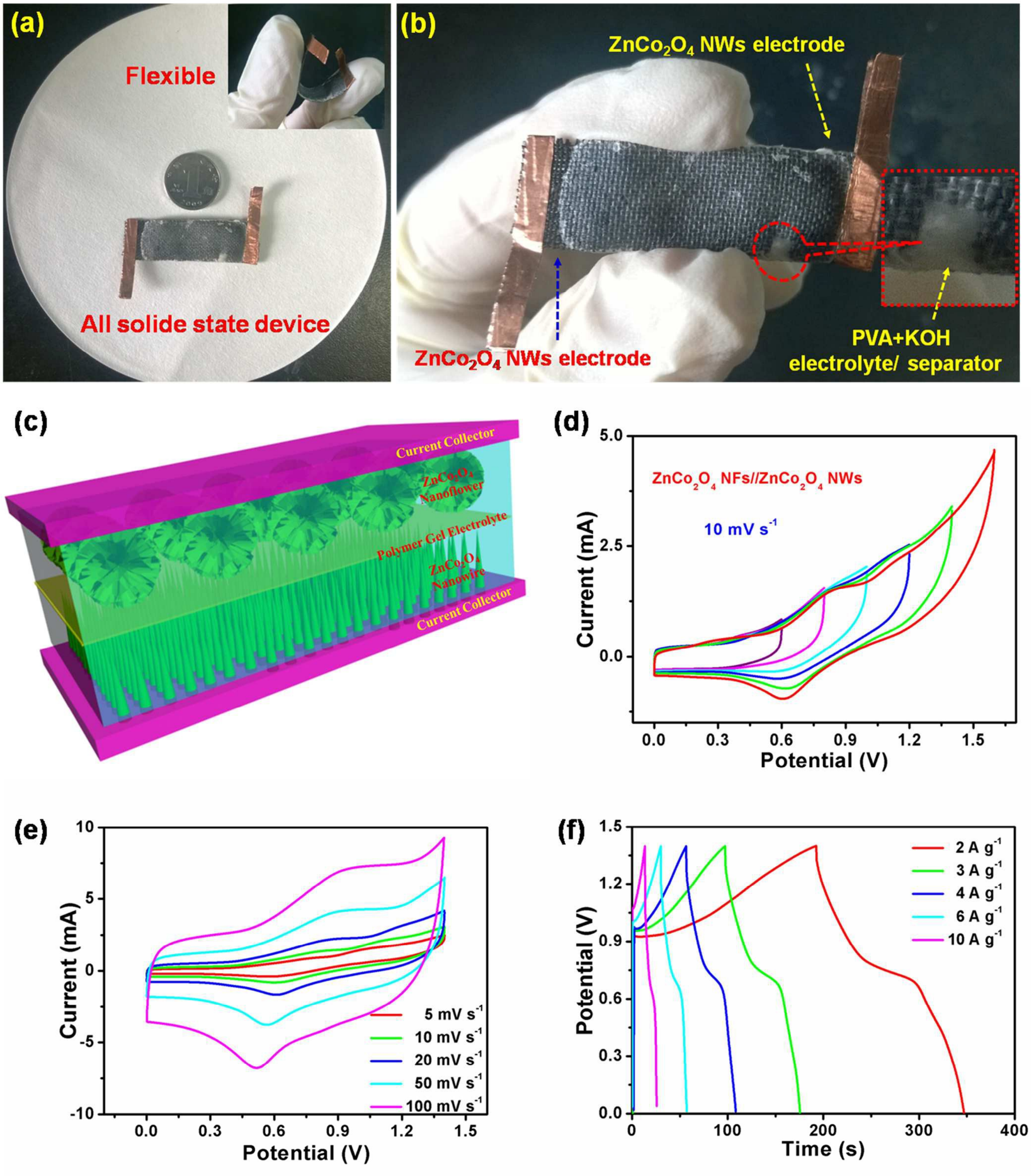

Figure 8. (a, b) Photographs of the device; (c) schematic illustration of the structure of the all-solid-state device; (d) CV curves acquired at different voltages at a scanning rate of 10 mV s^{-1}; (e) CV curves measured at scanning rates of 5, 10, 20, 50, and 100 mV s^{-1}at voltages between 0 and 1.4 V; (f) GCD curves of the device at different current densities.

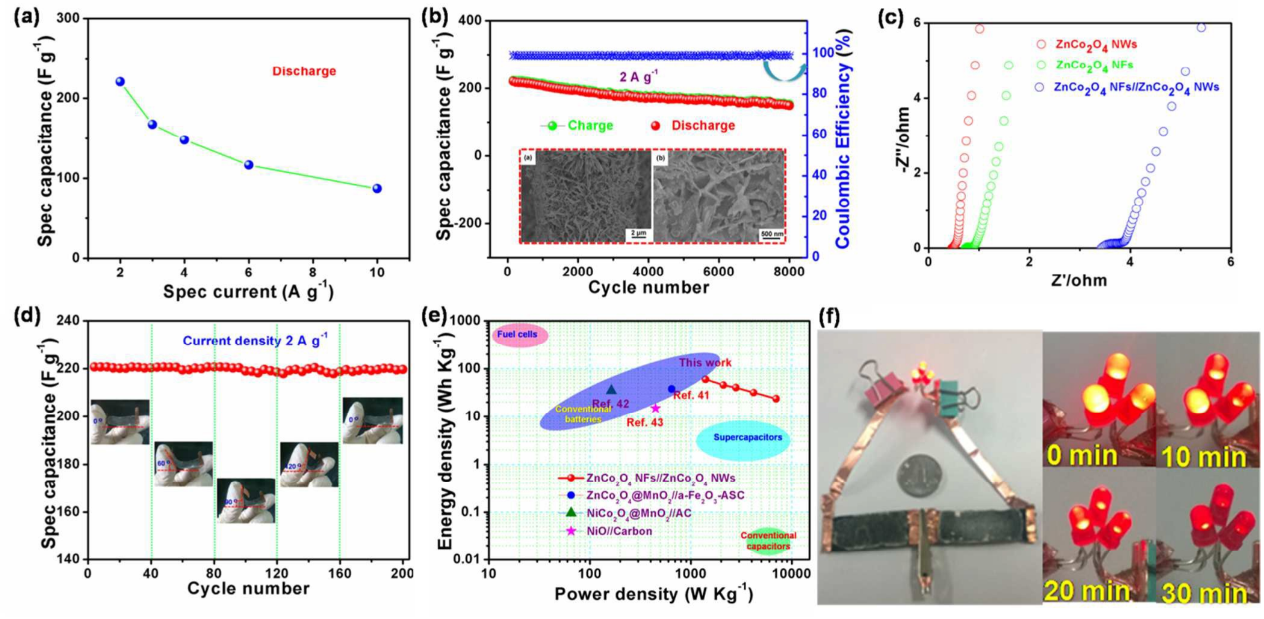

Figure 9. (a) Calculated specific capacities; (b) cycling performance of the device at a current density of 2 A g^{-1} for 8,000 cycles; (c) electrochemical impedance spectra (EIS) of the ZnCo$_2$O$_4$ NWs, ZnCo$_2$O$_4$ NFs and ZnCo$_2$O$_4$ NFs //ZnCo$_2$O$_4$ NWs electrodes; (d) Influence of the bending-induced mechanical stress upon specific capacitance; (e) Ragone plots of the device in comparison with other recently reported values from SCs; (f) optical images of three red LEDs powered by two all solid-state SCs connected in series.

Graphical Abstract

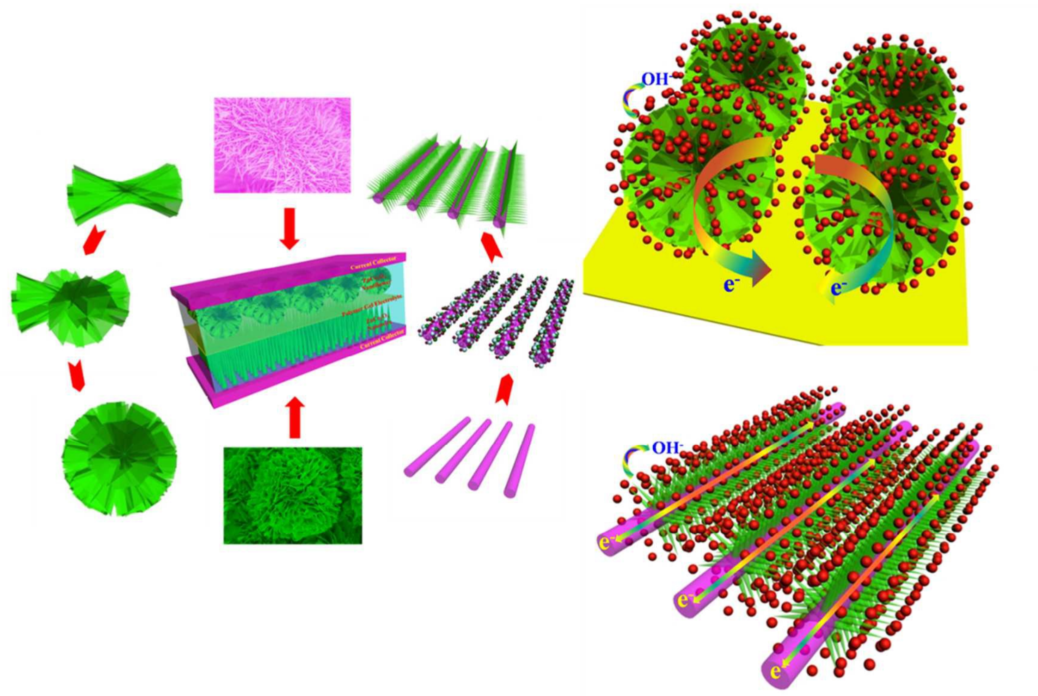

A $ZnCo_2O_4$ NFs//$ZnCo_2O_4$ NWs symmetrical device is designed and prepared. Theoretical assessment confirms the rationality of the experimental scheme and explains the increased band gap. The fabricated device possesses advantages such as a small size and excellent flexibility and has large potential in lightweight and flexible energy storage applications.